J. Phys. Chem. A **1997,** *101,* 6583−6592 **6583**

Photodissociation spectroscopy and dynamics of CH_3O and CD_3O

David L. Osborn,† David J. Leahy, and Daniel M. Neumark*

Department of Chemistry, University of California, Berkeley, California 94720, and Chemical Science Division, Lawrence Berkeley National Laboratory, Berkeley, California, 94720

Received: February 25, 1997⊗

The photodissociation spectroscopy and dynamics of the methoxy radical $\tilde{A}(^2A_1) \leftarrow \tilde{X}(^2E)$ transition have been investigated using fast radical beam photofragment translational spectroscopy. The $\tilde{A}$ state of both CH_3O and CD_3O is observed to predissociate via curve crossings with one or more repulsive electronic states. The photofragment yield spectrum consists of the C−O stretch progression and combination bands based on this mode. The major product channel is CH_3 (CD_3) + O, with a threshold 3775 cm^{-1} above the zero-point level of the $\tilde{A}$ state. The product translational energy distributions reveal ν_2 umbrella excitation in CH_3 (CD_3), yielding considerable insight into the dissociation dynamics for this channel. CD_3O shows a mode-specific dynamical effect in which energy deposited in parent umbrella motion preferentially populates umbrella motion in the fragment. The product channels CH_2 + OH (CD_2 + OD) and D + CD_2O are also observed, with evidence that the methylene fragment is predominantly in the excited $\tilde{a}(^1A_1)$ state.

I. Introduction

The methoxy radical (CH_3O) is a remarkable molecule and has become one of the most widely studied polyatomic free radicals since it was first observed in emission of ethyl nitrate photolysis in 1953.[1] Methoxy has drawn such intense scrutiny because it serves as a paradigm for a surprisingly large number of fundamental physical and chemical interactions. It is important in the atmosphere due to its participation in smog chemistry[2] and is an intermediate in the combustion of cool flames of methane,[3] oxygenated fuels containing CH_3OH, and fuel-lean ignition processes.[4] Although not yet detected in interstellar gas, it is quite likely that CH_3O exists in this medium because its close relatives CH_3OH and CH_2O are found in abundance.[5]

In the field of photodissociation dynamics, the rich photochemistry of methoxy provides archetypal cases of two distinct dissociation mechanisms. On the ground state surface, dissociation to H + CH_2O is impeded by an activation barrier. Stimulated emission pumping (SEP) experiments show narrow resonances both below and above the barrier, addressing the long-standing question of mode-specific *vs* statistical unimolecular decomposition.[6] In a preliminary report,[7] we presented the first unambiguous evidence for predissociation of CH_3O following excitation of the ultraviolet $\tilde{A}(^2A_1) \leftarrow \tilde{X}(^2E)$ transition. In contrast with barrier-impeded ground state dissociation, UV dissociation of methoxy, yielding CH_3 + O, provides a textbook example of predissociation via coupling to purely repulsive excited state potential energy surfaces. In this paper we give a full exposition covering our experiments on the ultraviolet photodissociation dynamics of CH_3O and CD_3O.

Although the literature on CH_3O is quite extensive, the most germane works from the viewpoint of photodissociation dynamics are the spectroscopic[6−31] and theoretical investigations[32−40] of the rotational, vibrational, and electronic structure of methoxy. Within the C_{3v} point group, the CH_3O ground state is of E symmetry due to a 2-fold electronic degeneracy. Consequently, CH_3O is subject to vibronic coupling via the Jahn−Teller effect[41,42] in which nuclear motion along one (or more) of the e symmetry vibrations splits the electronic degeneracy. In addition, the unpaired electron spin can couple to the magnetic field generated by the electronic orbital motion around the symmetry axis. As a result, methoxy is a prototypical example of the complications that arise when both Jahn−Teller and spin−orbit effects must be treated together.[43]

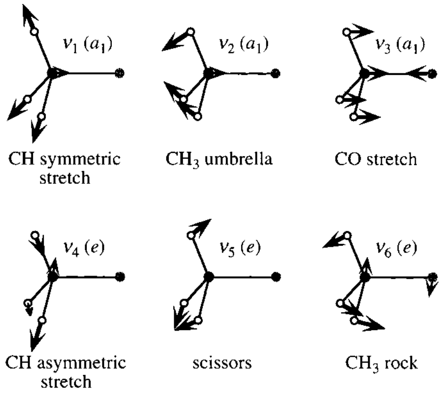

Figure 1. Vibrational normal modes of CH_3O.

The spectroscopy of CH_3O is far from straightforward, with a substantial amount of controversy surrounding the proper values of the spectroscopic parameters. As noted by Foster *et al.*,[23] there has been a great deal of confusion in determining the true location of the 0_0^0 band in the $\tilde{A}(^2A_1) \leftarrow \tilde{X}(^2E)$ transition. These difficulties arise in part from the fact that all three non-totally symmetric (e) vibrations (ν_4, ν_5, and ν_6) are active in the $\tilde{A}$ state, in addition to the three totally symmetric (a_1) vibrations (ν_1, ν_2, and ν_3); the normal modes for the six vibrations are shown in Figure 1. The resulting spectra are rather complex, even at the very low rotational and vibrational temperature achieved in a supersonic jet expansion. Extensive vibrational[30] and rotational[25,30] analyses of the $\tilde{A} \leftarrow \tilde{X}$ laser-induced fluorescence (LIF) spectrum give the accepted value of the rovibronic band origin $T_0 = 31\,614.51$ cm^{-1}.

All experimental and theoretical investigations agree that the main progression in the $\tilde{A} \leftarrow \tilde{X}$ transition is the 662 cm^{-1} ν_3 mode, the C−O stretch. The extended Franck−Condon progression in this mode arises from the large change in C−O bond length between ground and excited states ($r_{CO}' = 1.58$ Å $\leftarrow$ $r_{CO}'' = 1.37$ Å).[25] The increase in r_{CO} results from excitation of a CO σ-bonding electron to a nonbonding p_π orbital localized

---

† Current address: JILA, Campus Box 440, Boulder, CO 80309-0440.

⊗ Abstract published in *Advance ACS Abstracts,* July 15, 1997.

S1089-5639(97)00696-8 CCC: \$14.00

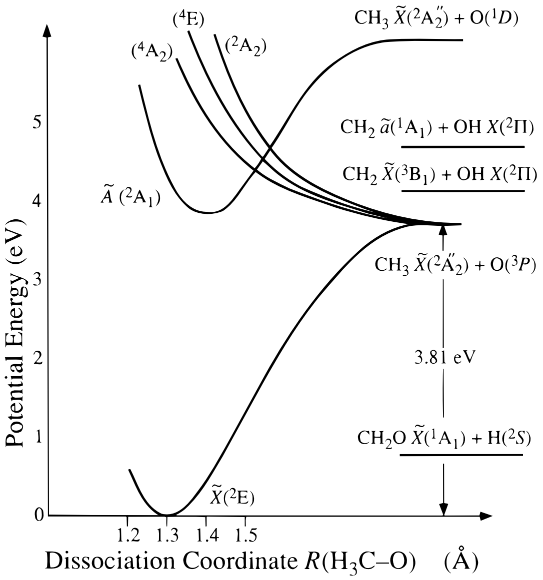

Figure 2. Schematic C_{3v} potential energy surfaces for the methoxy radical as a function of CO bond length.

on the oxygen atom, leaving essentially half a CO bond in the $\tilde{A}(^2A_1)$ state. However, due to the complexity of the spectrum, the vibrational frequencies for several of the other modes have proved difficult to evaluate, although two recent investigations appear to have settled all the major discrepancies.[30,31] There has also been considerable variation in the reported values of the $\tilde{A}$ state fluorescence lifetime.[12,17–19,22] The most recent measurements (obtained under collisionless conditions) for the ν_3 progression give $\tau_{FL}(3^n_0,\ n < 6) \approx 2\ \mu s$, $\tau_{FL}(3^6_0) = 0.35$–$0.38\ \mu s$, and $\tau_{FL}(3^7_0) < 0.02\ \mu s$.[44]

Jackels performed the first systematic theoretical investigation of the many excited electronic states of CH_3O.[33] In addition to the bound $\tilde{X}(^2E)$ and $\tilde{A}(^2A_1)$ states, he reported three electronic states of $^4A_2$, ^4E, and $^2A_2$ symmetry which are purely repulsive along the C–O coordinate, shown schematically in Figure 2. The curve crossing between the lowest of these states and the $\tilde{A}$ state was predicted to lie at 36 500 cm^{-1}, slightly above the energy of the 3^7_0 transition. More detailed *ab initio* investigations, including the coupling strengths between different excited electronic states, have recently been undertaken by Pederson and Yarkony[39] and by Cui and Morokuma.[40]

There are at least four photodissociation product channels open to methoxy at the excitation energies used in this study:

$$CH_3O(\tilde{X}(^2E)) \xrightarrow{h\nu} CH_3O(\tilde{A}(^2A_1)) \rightarrow$$

$$CH_3(\tilde{X}(^2A_2'')) + O(^3P) \qquad \Delta H_{rxn,0} = 3.807 \pm 0.013 \text{ eV} \qquad \text{(I)}$$

$$CH_2(\tilde{X}(^3B_1)) + OH(\tilde{X}(^2\Pi)) \qquad \Delta H_{rxn,0} = 4.10 \pm 0.05 \text{ eV} \qquad \text{(II)}$$

$$CH_2(\tilde{a}(^1A_1)) + OH(\tilde{X}(^2\Pi)) \qquad \Delta H_{rxn,0} = 4.49 \pm 0.05 \text{ eV} \qquad \text{(III)}$$

$$CH_2O(\tilde{X}(^1A_1)) + H(^2S) \qquad \Delta H_{rxn,0} = 0.78 \pm 0.07 \text{ eV} \qquad \text{(IV)}$$

The energetics are based on the heat of formation of methoxy $\Delta H°_{f,0}(CH_3O) = 0.29 \pm 0.02$ eV (6.8 ± 0.4 kcal/mol) found in our preliminary investigation[7] and the literature values for other species.[45] Channel I is the major product channel for CH_3O at all photon energies. The formation of $CH_2 + OH$ via channels II and/or III is observed as a minor product channel in CH_3O photodissociation. The corresponding channels are also observed with CD_3O. As discussed elsewhere,[46] detection of H atom loss is difficult though not impossible with our apparatus. For methoxy we have evidence that channel IV plays a very minor role in methoxy dissociation at high photon energies.

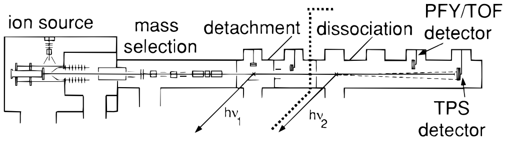

Figure 3. The fast radical beam translational spectrometer. The dotted line separates the radical production section on the left from the photodissociation section on the right. The flight distance L between the dissociation laser and a detector is 0.68 m for the TOF detector and either 1.00 or 2.00 meters for the TPS detector.

Our experimental results for both isotopes are presented in section III and analyzed in section IV. In section V we discuss the dissociation dynamics of methoxy in light of the experimental distributions and comment on the possibilities for further investigations.

II. Experimental Section

The experimental apparatus used in these studies, the fast beam photofragment translational spectrometer (Figure 3), has been described in detail elsewhere, [47,48] and only a brief description is given here. In order to produce a well-characterized sample of free radicals, we rely on the fact that open-shell species have positive electron affinities and form stable negative ions. The neutral free radical of interest is generated by laser photodetachment of the mass-selected negative ion precursor and subsequently photodissociated by a second laser:

$$CH_3O^- \xrightarrow{h\nu_1} CH_3O + e^- \xrightarrow{h\nu_2} \text{fragments} \qquad (1)$$

Consequently, the apparatus in Figure 3 is divided into two main regions. In the first region ions are generated and photodetached, while radical photodissociation occurs in the second region.

Methoxide ions are formed in a 60 Hz pulsed supersonic expansion of CH_3OH seeded in 5 atm Ne at room temperature. A pulsed electric discharge in the throat of the expansion creates negative ions,[49] which cool both rotationally and vibrationally during the expansion. The ions are accelerated to 8000 eV laboratory energy and mass selected by the Bakker time-of-flight (TOF) method.[50] The output of a pulsed dye laser intersects the ion beam at the appropriate time such that only methoxide ions are photodetached. Furthermore, the detachment energy is just above threshold[9] ($h\nu = 1.71$ eV for CH_3O, $h\nu = 1.66$ eV for CD_3O), so that methoxy is created only in its ground vibrational state.

In the second region of the apparatus, a frequency-doubled pulsed dye laser, operating between 35 000–40 500 cm^{-1} with a bandwidth of 0.3 cm^{-1}, intersects the packet of methoxy radicals. The dissociation laser is calibrated against the absorption spectrum of I_2,[51] with an absolute accuracy of 1 cm^{-1}. Fragments from a photodissociation event are detected directly, without an ionization step, using one of two microchannel plate (MCP) detectors. An aluminum strip across the center of each detector prevents undissociated radicals from striking the MCPs, so that all signal observed is due to recoiling photofragments.

Three types of experiments are performed to characterize the photodissociation of methoxy. First, photofragment yield (PFY) spectra are obtained by monitoring the total flux of fragments

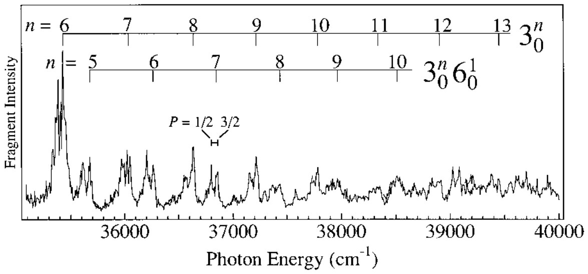

Figure 4. Photofragment yield spectrum of CH_3O. The 60 cm^{-1} spin−orbit splitting between the ^2E_P, $P = {}^3/_2, {}^1/_2$ levels of the $\tilde{X}$ state is shown.

at the TOF detector, located 0.68 m from the dissociation laser, as a function of laser wavelength. The resulting spectrum is complementary to absorption and fluorescence measurements.

Second, after the PFY spectrum is acquired, the photodissociation laser is fixed at a specific energy, and both fragments arising from a single parent radical are detected in coincidence using a time- and position-sensitive (TPS) wedge- and strip-anode detector,[52,53] located 2.0 m from the dissociation laser. Due to the favorable kinematics of this fast beam experiment, the data may be directly inverted to produce the two-dimensional-coupled translational energy and angular distribution $P(E_T,\theta)$ where E_T is the center-of-mass relative translational energy of the recoiling fragments and θ is their scattering angle with respect to the electric field of the linearly polarized dissociation laser. This distribution can be separated according to

$$P(E_T,\theta) = P(E_T)\{1 + \beta(E_T)P_2(\cos\theta)\} \qquad (2)$$

into the angle-independent translational energy distribution $P(E_T)$ and the energy-dependent anisotropy parameter[54] $\beta(E_T)$, which describes the angular distribution of fragments. The high laboratory kinetic energy of the fragments affords an MCP detection efficiency of $\approx$ 50%, which is independent of the identity of the fragment (except for H or D atoms, as noted below). For the experiments presented here, the translational energy resolution is given by $\Delta E_T/E_T = 2.2\%$. This coincidence detection scheme is only feasible when the mass ratio of the two fragments $m_1/m_2 \leq 5$.

Because of this restriction, detection of channel IV requires a different approach. The third mode of operation is a noncoincidence experiment, in which the time-of-flight of the photofragments is recorded by digitizing the signal from the TOF detector in 1 ns time bins.[46] The observable is a projection of the 3-D velocity distribution onto the radical beam axis, averaging out much of the detail which is present in the full $P(E_T,\theta)$ distribution. In exchange for this sacrifice of detail, hydrogen atom loss channels are particularly distinct because of the large spread in flight times for H (or D) atoms scattered parallel and antiparallel to the ion beam direction. Given sufficient data, a Monte Carlo forward convolution routine can be implemented to determine translational energy and angular distributions which are consistent with the TOF data. In practice, the experiment is much more sensitive to D atoms than H atoms, and this experiment has only been performed for CD_3O. Even for D atoms, the detection efficiency of $\approx$8% is significantly reduced from that of "heavy" fragments such as CH_3.

III. Results

A. Photofragment Yield Spectra of CH_3O and CD_3O. The PFY spectrum shown in Figure 4 (first reported in ref 7) is a direct observation of photodissociation in the $\tilde{A}(^2A_1) \leftarrow \tilde{X}(^2E)$ transition. The spectrum is composed of two prominent vibrational progressions superimposed on a small but finite continuum of photofragment signal. No signal was observed below 35 300 cm^{-1}. Rotational resolution was not a priority in this study, and although it has been resolved, such spectra are very congested, in part due to the estimated rotational temperatures of 35−50 K in the radical beam.[52,55] Therefore, a relatively large laser step size of $\approx$6 cm^{-1} was adopted to allow increased signal averaging at each photon energy. However, because of the underlying rotational structure, each individual scan was offset slightly in energy from the previous data in a given scan range in order to average over rotational features, which might otherwise provide spurious structure since the laser step size is larger than the laser bandwidth (0.3 cm^{-1}).

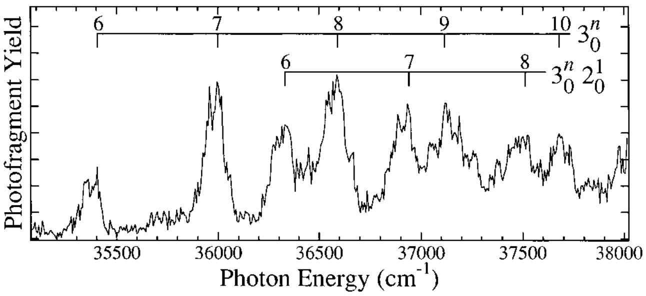

Figure 5. Photofragment yield spectrum of CD_3O.

The two progressions in Figure 4 have a spacing of $\approx$ 600 cm^{-1}, implicating progressions involving ν_3, the CO stretch (see Figure 1). The CO stretching mode also dominates the absorption and LIF spectra, where it has a fundamental frequency of ν_3 = 662 cm^{-1}.[30] The two progressions we observe are assigned as the pure CO stretch, 3^n_0 (n = 6−13), and a combination band $3^n_0 6^1_0$ (n = 5−10), which involves one quantum of the nontotally symmetric methyl rock vibration. The assignment of the combination band differs from that presented in our preliminary investigation[7] and is discussed in section IV.A. On a finer scale, each peak shows a splitting of approximately 60 cm^{-1} (see Figure 4), corresponding to the spin−orbit splitting between the $^2E_{3/2}$ and $^2E_{1/2}$ components of the ground electronic state. Both spin components are present because each represents an allowed transition in the photodetachment of $CH_3O^-(^1A_1)$. However, the "hot" spin−orbit distribution does not imply a hot vibrational distribution. In fact, the photoelectron spectrum of CH_3O^- (acquired on a different apparatus but with the same ion source) shows no hot bands, implying that all the ions are in their vibrational ground state.[56] To aid in comparison with LIF spectra[13,16,23−28,30] of jet-cooled methoxy, which probed only transitions from the lower $^2E_{3/2}$ component of the ground state, the vibrational combs in Figure 4 are centered on those transitions originating in the $^2E_{3/2}$ component.

Figure 5 shows the corresponding PFY spectrum for the CD_3O radical. The general features of the spectrum are analogous to CH_3O, 3^n_0 is the main progression and is accompanied by a combination band. However, the continuum signal underneath the vibrational structure is more intense at lower energies for CD_3O than for CH_3O. In addition, the combination band observed for CD_3O is assigned to a different progression involving umbrella motion, $3^n_0 2^1_0$, as discussed in section IV.A.

B. Translational Energy and Angular Distributions. The photofragment translational energy distributions $P(E_T)$ arising from CH_3O and CD_3O, are given in Figures 6 and 7 for excitation of several vibrational levels shown in the PFY spectra of Figures 4 and 5, respectively. The translational energy is binned in intervals of 10 meV. For photon energies $h\nu$ < 37 500

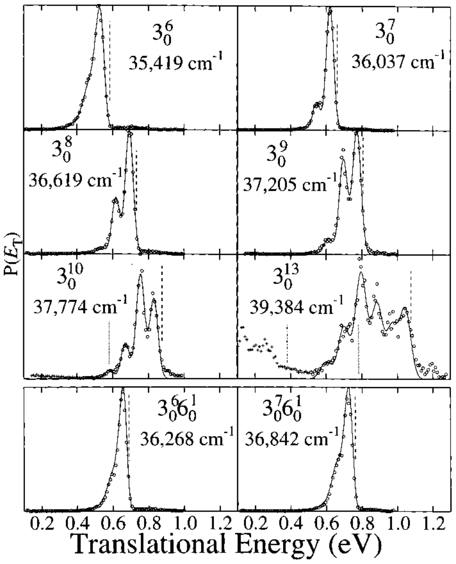

Figure 6. $P(E_T)$ distributions for CH_3O. Circles show $CH_3 + O$ data, crosses show $CH_2 + OH$ data, while the line represents the fit to $CH_3 + O$ discussed in the text. Thermodynamic thresholds are given for $CH_3 + O$ (– –), CH_2 $\tilde{X}(^3B_1)$ + OH (···), and CH_2 $\tilde{a}(^1A_1)$ + OH (· –).

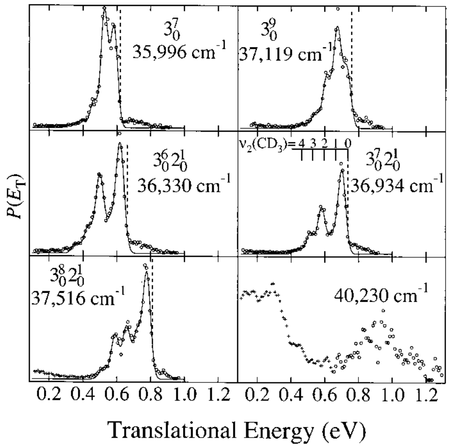

Figure 7. $P(E_T)$ distributions for CD_3O. The legend is identical to Figure 6.

cm^{-1}, all signal arises from simple C–O bond fission, *i.e.*, channel I. Most of the available energy is deposited into translation of the recoiling fragments, because the distributions peak near the maximum translational energy available (see section IV.B) as denoted by the dashed vertical line in each distribution of Figures 6 and 7. The most striking feature in the CH_3O $P(E_T)$ distributions is the progression with a spacing of ≈74 meV (600 cm^{-1}), which is easily seen in the 3^n_0 data sets ($n \geq 7$). As detailed in section IV.B, these features arise from excitation of the ν_2 umbrella mode of the CH_3 fragment. Note that the vibrational features are much less distinct in the $P(E_T)$ distributions from the 3^6_0 and $3^n_0 6^1_0$ bands.

In the CD_3O $P(E_T)$ distributions (Figure 7), most of the available energy again goes into product translation, with a product vibrational progression of ≈57 meV (460 cm^{-1}) observed, corresponding to excitation of the ν_2 umbrella mode in CD_3 photofragment. The most surprising results in Figure 7 are the product state distributions observed when the $3^n_0 2^1_0$ combination band is excited. In section IV.B, we will show that these $P(E_T)$ distributions are the result of a bimodal distribution in the ν_2 mode of CD_3, with the two most intense peaks corresponding to $v_2 = 0$ and $v_2 = 2$. Note the stark contrast between the distributions arising from $3^n_0 2^1_0$ excitation of CD_3O and those arising from $3^n_0 6^1_0$ excitation of CH_3O.

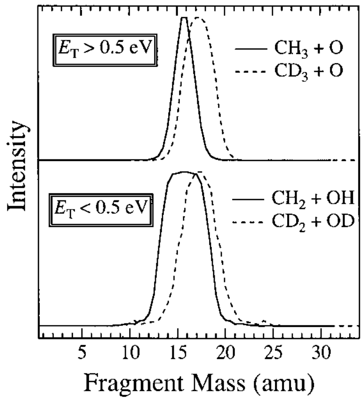

Figure 8. Photofragment mass spectrum exciting 3^{13}_0 of CH_3O (—) and 40 230 cm^{-1} of CD_3O (···). Note that for $E_T > 0.5$ eV, the deuterium isotope has the broader fwhm, implying fragmentation to channel I, while for $E_T < 0.5$ eV the hydrogen isotope has the broader fwhm, implying fragmentation to channels II and/or III. The peak heights are normalized to unity and do not represent branching ratios.

All of the $P(E_T)$ distributions presented arise from excitation of the $^2E_{3/2}$ level of the $\tilde{X}$ state. Excitation from the $^2E_{1/2}$ levels exhibits identical behavior, which is to be expected since the level excited in the $\tilde{A}(^2A_1)$ state is identical. In addition, $P(E_T)$ distributions acquired at three different photon energies within the rotational envelope of the 3^8_0 band of CH_3O show no significant differences. Therefore, further investigations of the dependence of the photodissociation dynamics on the excited state rotational level were not pursued.

For $h\nu > 37\,500$ cm^{-1}, the structured features in the $P(E_T)$ distributions arising from C–O bond fission remain, but a new feature is observed in both isotopes for $E_T < 0.5$ eV which is due to production of $CH_2 + OH$ ($CD_2 + OD$). The evidence for this new channel is shown in Figure 8, which gives the product mass spectra of CH_3O and CD_3O for 3^{13}_0 and 40 230 cm^{-1} excitation respectively, divided into contributions for $E_T > 0.5$ eV and $E_T < 0.5$ eV. The comparison between the two isotopes is useful because the product mass resolution is not sufficient to unambiguously resolve peaks arising from CH_2, CH_3, O, and OH. Although only a single peak appears in the mass spectra, the width of this peak depends on the product masses.

For CD_3O the two fragments have masses 16 and 18 *regardless* of whether channel I ($CD_3 + O$) or channel II/III ($CD_2 + OD$) is produced, resulting in an identical product mass spectrum regardless of the branching ratio between these two channels. In CH_3O, the analogous decay pathways have product masses 15 and 16, or 14 and 17, respectively. Therefore, formation of channel I should give rise to a narrower peak for CH_3O than for CD_3O, while channel II/III products will give a broader peak for CH_3O than for CD_3O. From these considerations, the only conclusion consistent with the results in Figure 8 is that channel I products dominate for $E_T > 0.5$ eV, while channel II/III products dominate when $E_T < 0.5$ eV.

The branching ratio of $CH_3 + O$:$CH_2 + OH$ decreases with photon energy and is 3:1 for 3^{13}_0. The same trend occurs in CD_3O, where the extreme case of excitation at $h\nu = 40\,230$ cm^{-1} results in a branching ration $CD_3 + O$:$CD_2 + OD$ of ≈1:1, as shown in Figure 7.

In all the data sets acquired for methoxy, the anisotropy parameter $\beta(E_T)$ is independent of E_T. For CH_3O, the 3^n_0 transitions show angular distributions which are isotropic to within experimental error, while the $3^n_0 6^1_0$ transitions are slightly anisotropic, described by $\beta = 0.4 \pm 0.1$ for $3^6_0 6^1_0$, and $\beta = 0.3 \pm 0.1$ for $3^7_0 6^1_0$. These positive values of β are unexpected for a perpendicular electronic transition and are discussed further in section V.B. In CD_3O, all the transitions give isotropic angular distributions within experimental error.

C. Noncoincidence Time-of-Flight Distributions. As mentioned in the experimental section, a noncoincidence experiment must be performed in order to assess the importance of the hydrogen atom loss pathway, channel IV. In our preliminary work on methoxy, we reported a branching ratio for channel IV in CD_3O of $2\%^{+5}_{-1}$, and $10\%^{+10}_{-5}$ for the 3^8_0 and 3^{10}_0 bands, respectively.[7] The experiments were repeated recently, and the data again show evidence of D atom loss from CD_3O, but with less intensity than our earlier data. On the basis of our experience with photodissociation of the vinoxy radical, in which D atom loss is a major channel,[46] it appears that the branching ratio for CD_2O + D is smaller than the values reported previously, representing no more than 5% of the branching ratio at 3^{10}_0. In any event, this decay channel seems to be of minor importance in methoxy, at least for the photon energy range used in this experiment.

IV. Analysis

A. Photofragment Yield Spectra of CH_3O and CD_3O. The rovibronic term value T_0 for the $\tilde{A}(^2A_1) \leftarrow \tilde{X}(^2E)$ transition in CH_3O was given by Liu *et al.*[25] as 31 614.51 cm^{-1} from rotational analysis of the combined LIF and microwave[14] data. The effective 0^0_0 transition, *i.e.*, including spin−orbit splitting, measured from the lowest level of the $^2E_{3/2}$ component of the ground state, is 31 644.6 cm^{-1}. It is convenient to use this value when comparing the vibronically resolved $\tilde{A}(^2A_1) \leftarrow \tilde{X}(^2E_{3/2})$ components in our PFY spectra with jet-cooled LIF experiments, in which all transitions originate from the $^2E_{3/2}$ component.

The significant increase in CO bond length for the $\tilde{A} \leftarrow \tilde{X}$ transition gives rise to an extended Franck−Condon progression in the ν_3 mode for both absorption and LIF measurements, and the same progression should dominate the PFY spectrum. While fluorescence is observed in CH_3O up to ≈37 000 cm^{-1}, spectroscopic assignments from LIF are complicated in this energy range due to spectral congestion and a Fermi resonance between ν_2 and $2\nu_3$ in the $\tilde{A}$ state. We assign the lowest energy dissociative transition as 3^6_0, corresponding to an energy 3775 cm^{-1} above the zero-point level of the $\tilde{A}$ state. This transition represents the first dissociative member of the 3^n_0 progression, which may also contain contributions from $3^{n-2}_0 2^1_0$, $3^{n-4}_0 2^2_0$, etc., due to the Fermi resonance. On the basis of the most recent rovibrationally resolved LIF data,[30] the 3^6_0 transition occurs at 35 437 cm^{-1}, compared with 35 419 cm^{-1} in our PFY spectrum. The comparison of LIF with PFY transition frequencies agrees to within experimental uncertainty when one considers that our rotational temperature (35−50 K) is greater than in the LIF spectra (5 K), displacing the band maxima (which we measure) from the true rovibronic origin. In addition, our laser step size of ≈6 cm^{-1} prevents us from determining band maxima more precisely than this value.

In our previous analysis of the PFY spectrum of CH_3O,[7] we assigned the combination band shown in Figure 4 as $3^n_0 5^1_0$, the only feasible assignment based on the accepted vibrational frequencies of the $\tilde{A}$ state at that time.[23] Due to a recent reassignment[30] of the ν_6 fundamental frequency in the $\tilde{A}$ state (previously 595 cm^{-1}, currently 929.5 cm^{-1}), it is unclear from the peak positions alone whether the combination band we observe in the PFY spectrum of CH_3O arises from the ν_5 (1403 cm^{-1}) or the ν_6 mode. The ambiguity arises because the $3^n_0 5^1_0$ and $3^{n+1}_0 6^1_0$ progressions have nearly identical frequencies. However, our dynamics results discussed in section V.B.1, together with recent fluorescence depletion spectroscopy results,[44] suggest that the combination band observed in dissociation involves the ν_6 methyl rocking mode rather than ν_5. The $3^5_0 6^1_0$ transition measured by LIF[30] occurs at 35 673 cm^{-1}, compared with 35 666 cm^{-1} in the PFY spectrum.

The PFY spectrum of CD_3O (Figure 5) shows some interesting differences from that of CH_3O. Assignment of the 3^n_0 progression is straightforward, due to the small isotope shift in this mode (ν'_3 = 663 cm^{-1}).[23] However, the combination band we observe is more difficult to assign. While one might expect that the same $3^n_0 6^1_0$ progression found in CH_3O will be active in CD_3O, this assignment gives poor agreement with the data. Specifically, the ν_5 fundamental in CD_3O is reported as 1047 cm^{-1},[23] and we estimate the ν_6 fundamental as 693 cm^{-1} (based on the measured isotope shift in ν_5). From our observation of the 3^6_0 transition at 35 404 cm^{-1}, we expect the $3^6_0 5^1_0$ transition at ≈ 36 451 cm^{-1}, which is in fact a minimum between two peaks in Figure 5, and the $3^6_0 6^1_0$ transition at ≈ 36 097 cm^{-1}, which lies on the blue edge of the 3^7_0 transition. By contrast, the ν_2 fundamental (CD_3O umbrella) is 971 cm^{-1}, from which the $3^6_0 2^1_0$ transition is predicted at ≈36 375 cm^{-1}, in better agreement with the first peak at 36 330 cm^{-1} in the strong combination band of CD_3O. Therefore, we assign the combination band in the PFY spectrum of CD_3O as $3^n_0 2^1_0$, an assignment corroborated by the dissociation dynamics discussed in section V.B.2.

B. Translational Energy Distributions. *1. CH_3O.* Analysis of the $P(E_T)$ distributions will focus primarily on the CH_3 + O product channel, for which the most detailed information is obtained. The main goals of the analysis are to determine (i) the best value of the bond dissociation energy $D_0(CH_3{-}O)$, (ii) the CH_3 fragment vibrational distribution, and (iii) a measure of rotational excitation of the CH_3 fragment. The major analysis results are unchanged from those presented previously,[7] but a fuller description of the analysis is given here.

The balance of energy for photodissociation of methoxy is given by

$$h\nu + E_{\mathrm{int}}(CH_3O) = D_0(CH_3{-}O) + E_T + E_V(CH_3) + E_R(CH_3) + E_{SO}(O\ ^3P_j) \quad (3)$$

where E_{int} is the most probable rotational energy of the parent radical, E_V and E_R are the product vibrational and rotational energy, and E_{SO} is the spin−orbit energy of the oxygen atom. On the basis of a rotational temperature of 50 K, we estimate $E_{\mathrm{int}}(CH_3O)$ = 35 cm^{-1}. We can determine D_0 since we measure E_T directly, but only if we locate an energy in the $P(E_T)$ distribution for which the last three terms of eq 3 are zero. The steep falloff in intensity on the high-energy side of each distribution in Figure 6 is evidence for this thermodynamic limit, in which all the available energy goes into product translation, forming $CH_3(v = 0, J = 0) + O(^3P_2)$. For each data set we obtain an independent estimate of D_0 by extrapolating to the energy where the $P(E_T)$ distribution reaches zero intensity. An average of these thresholds, deconvoluted from the experimental resolution, gives the best value of $D_0(CH_3{-}O) = 3.807 \pm 0.013$ eV. From the known heats of formation of CH_3 and O,[45] we obtain the heat of formation $\Delta H^\circ_{f,0}(CH_3O) = 0.29 \pm 0.02$ eV (6.8 ± 0.4 kcal/mol). Additional thermodynamic quantities are derived from this value in ref 7.

In order to determine the product vibrational distributions, the data are fit to a set of rotational/spin−orbit distribution functions separated by the accurately known term energies of the CH_3 umbrella mode.[57] The distribution functions $f_n(E_T)$ are

TABLE 1: Product Branching Ratio for $CH_3O \rightarrow CH_3 + O$

transition	$h\nu^a$ (cm^{-1})	fwhm^a (meV)	$\langle E_V \rangle^b$ (meV)	$v = 0$	$v = 1$	$v = 2$	$v = 3$	$v = 4$	$v = 5$
3^6_0	35,419	68/63	12	84	14	1	0	0	0
3^7_0	36,037	47/39	14	82	16	1	0	0	0
3^8_0	36,619	50/41	26	67	28	3	1	0	0
3^9_0	37,205	53/43	44	52	40	7	1	0	0
3^{10}_0	37,774	53/43	73	35	45	16	4	1	0
3^{13}_0	39,384	73/70	179	19	15	20	28	14	4
$3^6_0 6^1_0$	36,268	53/45	10	87	11	1	0	0	0
$3^7_0 6^1_0$	36,842	58/50	14	80	17	1	0	0	0

[a] fwhm of vibrational peaks after deconvolution of experimental resolution. The left value in this column assumes production of only $O(^3P_2)$, while the right value assumesa statistical $O(^3P_j)$ distribution (see text). [b] Average vibrational energy.

TABLE 2: Product Branching ratio For $CD_3O \rightarrow CD_3 + O$

transition	$h\nu$ (cm^{-1})	fwhm^a (meV)	$\langle E_V \rangle^b$ (meV)	$v = 0$	$v = 1$	$v = 2$	$v = 3$	$v = 4$	$v = 5$
3^6_0	35,404	80	62	37	38	14	7	4	0
3^7_0	35,996	47	48	39	46	10	4	1	0
3^8_0	36,590	51	65	28	47	17	5	2	1
3^9_0	37,119	52	70	25	43	23	7	2	0
3^{10}_0	37,679	63	88	18	39	28	10	4	1
$3^6_0 2^1_0$	36,330	57	74	43	11	31	11	4	0
$3^7_0 2^1_0$	36,934	51	69	47	11	27	12	3	0
$3^8_0 2^1_0$	37,516	52	79	41	17	20	17	4	1

[a] fwhm of vibrational peaks after deconvolution of experimental resolution. [b] Average vibrational energy.

nearly Gaussian in shape,[58] with an asymmetric tail extending to lower translational energy, *i.e.*, toward higher rotational energy. The shape of this function is identical for every vibrational peak in a given spectrum. The model distribution, $F(E_T)$ is given by

$$F(E_T) = \sum_{n=0}^{n'} \alpha_n f_n \{E_T - (h\nu - D_0 - n\omega_2 - \Delta);\Gamma\} \quad (4)$$

Here n labels the number of quanta in the CH_3 ν_2 umbrella mode, Γ is the fwhm of the combined rotational/spin−orbit envelope and instrumental resolution, and Δ is the energy difference between the maximum possible E_T for each n $\{E_T^{max}(n) = h\nu - D_0 - n\omega_2\}$ and the peak of the nth rotational distribution function. The coefficients α_n give the CH_3 product vibrational distribution, while the instrumental resolution can be deconvoluted from the width Γ to give an indication of the energy balance between the last two terms of eq 3.[59]

The solid line in Figure 6 shows the best nonlinear least-squares fit to each data set, with the results given in Table 1. We note that the fits are sensitive to the strong negative anharmonicity in the ν_2 mode of CH_3, confirming our assignment that the highest energy peak in each spectrum corresponds to $v_2 = 0$. The third column of Table 1 shows the fwhm of the rotational envelope in meV for two limiting cases. The larger values fit the data under the assumption that all O atoms are produced in their $^3P_2$ ground state, while the smaller values result from assuming a statistical 5:3:1 population of the $^3P_{2:1:0}$ spin−orbit states (which have energies of 0:20:28 meV,[60] respectively). Both limits reproduce the data well, implying that this data is not sufficiently sensitive to distinguish between the two cases.

Finally, we consider product state distributions for channels II and III, producing $CH_2 + OH$, which are observed in the energy range $E_T < 0.5$ eV upon excitation of 3^{10}_0 and 3^{13}_0. While there is no reproducible vibrational structure in this data, we can speculate on the relative importance of $CH_2(\tilde{X}(^3B_1))$ *vs* $\tilde{a}(^1A_1)$. Referring to Figure 6, any data with $E_T > E^T_{max}$ III can only be due to fragmentation via channel II. For $E_T < E^T_{max}$ III, both channels can contribute, but the significant rise in the signal concurrent with the opening of the electronically excited methylene channel implies that channel III is the major source of $CH_2 + OH$. While it is energetically possible that the data with $0.6 < E_T < 0.78$ eV for 3^{13}_0 is due to channel II, the mass spectrum for this energy range implies that this data arises from $CH_3 + O$, as denoted by the symbols in Figure 6.

2. *CD_3O.* A similar data analysis is undertaken for the $CD_3 + O$ product channel in the deuterated species, with the results given in Table 2. Deuteration lowers the frequency of the methyl radical umbrella mode from 606 to 458 cm^{-1},[61] which explains the less-resolved vibrational structure observed in the top two panels of Figure 7. Two important differences are observed in comparison to CH_3O dissociation. First, for a given level of excitation in the 3^n_0 progression, the CD_3 vibrational distributions are substantially hotter than those observed for CH_3. Second, the vibrational distributions for the $3^n_0 2^1_0$ series are bimodal, with the population of $v_2 = 0$ and $v_2 = 2$ always greater than that for $v_2 = 1$. The origin of these effects will be discussed in the next section. Fitting all the data sets for CD_3O gives the best value of $D_0(CD_3{-}O) = 3.85 \pm 0.02$ eV, and therefore $\Delta H°_{f,0}(CD_3O) = 0.16 \pm 0.04$ eV (3.7 ± 0.9kcal/mol).[62] Note the significant difference of 0.13 eV (3.1 kcal/mol) compared to the heat of formation of CH_3O, reflecting differences in vibrational frequencies between the H and D isotopes.

V. Discussion

A. Photofragment Yield Spectra of CH_3O and CD_3O. One of the important conclusions from the PFY spectrum is that, within our detection limits, CH_3O does not dissociate for photon energies below the 3^6_0 transition. This threshold implies that the crossing of the $\tilde{A}$ state by the lowest of the three repulsive curves shown in Figure 2 occurs in the vicinity of 3775 cm^{-1} above the $\tilde{A}$ state zero-point level. The onset of dissociation and the energy of the curve crossing has been the subject of much debate among both experimentalists and theorists, with our value being the lowest reported. Our threshold is unambiguous because we detect dissociation directly by measuring the presence of primary photofragments. A very recent determination of the dissociation threshold by Powers *et* *al.*,[44] via LIF lifetime measurements and fluorescence depletion spectroscopy (FDS), gives 3793 cm^{-1}, in good agreement with our value.

One of the main complexities in the $\tilde{A}(^2A_1)$ state of CH_3O arises because two quanta of ν_3 establish a Fermi resonance with ν_2 (CH_3O umbrella, 1289 cm^{-1}), giving rise to a series of multiplets at each overtone in the 3_0^n series.[16] By fitting the observed multiplet spectra to an anharmonic oscillator Hamiltonian for ν_2 and ν_3, Powers *et al.*[30] obtained the dominant character of each member of the Fermi multiplet. An interesting question is whether the competition between predissociation and fluorescence depends on which member of the multiplet is excited, in which case the PFY and LIF spectra would differ. If mixing between ν_2 and ν_3 is not too strong, one might expect that components of predominantly ν_3 character would dissociate more readily than those with more ν_2 character.

The splittings between Fermi multiplet components are significant. For example, the 3_0^5, $3_0^1 2_0^2$, and $3_0^3 2_0^1$ bands are separated by 35 and 43 cm^{-1}, respectively,[30] giving a total width to this feature of 78 cm^{-1}. However, the peak widths in the PFY spectrum (Figure 4) are also broadened due to the width of the rotational bands (at least 20 cm^{-1}) and the fact that we observe transitions from both $^2E_{3/2}$ and $^2E_{1/2}$ components ($\Delta E \approx 60$ cm^{-1}) of the ground state. It is therefore difficult to determine whether different multiplet components decay with different rates from the PFY spectrum. In fact, the LIF and FDS experiments of Powers *et al.*[44] show no significant differences in lifetimes for different members of a particular multiplet, indicating that ν_2 and ν_3 are indeed strongly mixed.

In CD_3O, the Fermi resonance between ν_2 and ν_3 is lifted, and the vibrational frequencies of all modes except ν_3 are substantially lowered. As a consequence, the $3_0^n 2_0^1$ combination band now appears as a distinct progression. The $3_0^6 2_0^1$ transition is the first member of this band seen in the PFY spectrum. While dissociation is energetically possible from excitation of the $3_0^5 2_0^1$ transition (expected at 35 670 cm^{-1}), this transition is not observed in Figure 5, implying that for CD_3O, energy deposited in ν_2 is not available to facilitate fragmentation. In contrast, CH_3O dissociates when the $3_0^5 6_0^1$ transition is excited, *i.e.*, with five quanta in ν_3. The isotopic comparison implies that excitation of the e symmetry vibration ν_6 (observed for CH_3O) promotes dissociation, while energy deposited in the a_1 symmetry ν_2 mode (observed for CD_3O) is not strongly coupled to the reaction coordinate. We give further evidence for these conclusions in section V.B., based on the translational energy and angular distribution data.

B. Channel I Dissociation Dynamics. Unimolecular photodissociation is a powerful technique because the disposal of energy among translation, vibrational, rotational, and electronic degrees of freedom in the products is a direct consequence of the potential energy surfaces on which this half-collision occurs.[63] Consequently, the main information we obtain on the dissociation dynamics of the methoxy radical is derived from the $P(E_T)$ distributions presented graphically in Figures 6 and 7 and numerically in Tables 1 and 2. In this section we discuss the dissociation mechanism for channels I−III in light of the experimental product state distributions.

1. $CH_3 + O$ Products. It is evident from Figure 6 that most of the available energy in the $\tilde{A} \leftarrow \tilde{X}$ photodissociation of CH_3O goes into product translation for channel I. Although radicals similar to methoxy, such as CH_2CHO, dissociate in the ultraviolet by internal conversion (IC) to the ground state potential energy surface (PES), the $P(E_T)$ distributions for methoxy are inconsistent with such a mechanism. Indeed, SEP studies[6] on CH_3O imply that, if IC were facile, $H + CH_2O$ would be the dominant product channel. Instead, the large recoil energies observed in our data are indicative of dynamics on a purely repulsive PES, in which potential energy is converted efficiently into translational kinetic energy. The results of *ab initio* calculations by Jackels,[33] represented schematically in Figure 2, predict three excited electronic states of $^4A_2$, ^4E, and $^2A_2$ symmetry, which are repulsive along the C−O bond and correlate asymptotically to $CH_3(\tilde{X}(^2A_2'')) + O(^3P)$. All our results for this channel are consistent with a mechanism in which non-adiabatic coupling between these surfaces and the optically prepared levels of the $\tilde{A}(^2A_1)$ state leads to predissociation of CH_3O. Given this basic description of the dissociation mechanism, we can explore further mechanistic details in the experimental data.

First, we consider the flow of energy into product vibration. Based on the fitting procedure presented in section IV.B., the $P(E_T)$ distribution is described accurately by excitation in a single CH_3 mode, the ν_2 umbrella vibration. Focusing on the 3_0^n progression, and ignoring for the moment $n = 6$, a smooth increase in the average CH_3 vibrational excitation $\langle E_V \rangle$ is observed with increasing photon energy (Table 1). Very little product excitation arises from the 3_0^7 level, in contrast to the inverted distributions for 3_0^{10} and 3_0^{13}.

The sudden approximation is often invoked to explain dissociation dynamics on purely repulsive surfaces. In this model the fragments are assumed to dissociate sufficiently rapidly that there is negligible coupling between translational and vibrational degrees of freedom. In the sudden limit, the CH_3 vibrational distribution is obtained by a Franck−Condon projection of the CH_3 moiety in the $\tilde{A}$ state onto the asymptotic ν_2 vibrational levels of the free methyl radical. Specifically, ∠HCO in the $\tilde{A}$ state is 106°, while asymptotically the methyl radical is planar, corresponding to $\angle HCO = 90°$ within C_{3v} symmetry. Using *ab initio* force constants for CH_3, the sudden approximation predicts a most probable value of $v_2 = 5$ for the CH_3 ν_2 distribution, somewhat hotter than the distribution observed at 3_0^{13} and clearly incorrect for all lower photon energies.

The failure of the sudden approximation implies substantial coupling of translational and vibrational degrees of freedom as the dissociation proceeds on the repulsive surface, allowing ∠HCO to relax smoothly with increasing CO bond length. In other words, at low photon energies, *e.g.*, 3_0^7 excitation, CH_3O appears to evolve adiabatically to products. This situation is entirely reasonable when one considers that the light H atoms can respond quickly to motion of the heavy C and O atoms as r_{CO} increases, maintaining an equilibrium value of ∠HCO at each value of r_{CO}. This picture also explains the behavior of the 3_0^n $P(E_T)$ distributions with increasing photon energy. The recoil velocity between the C and O atoms increases with increasing available energy, such that the H atoms cannot respond as accurately to the changing potential along the ∠HCO coordinate, resulting in increased asymptotic CH_3 vibrational excitation.

The photodissociation dynamics of methyl iodide show a strong similarity to our results on methoxy. For the $CH_3I \rightarrow CH_3 + I^*$ channel, which occurs on a purely repulsive surface, the methyl fragment is produced with little vibrational or rotational excitation. An adiabatic mechanism very similar to that described above for methoxy governs the dynamics of this channel in CH_3I, as elucidated by classical trajectory calculations on *ab initio* potential energy surfaces for this system.[64]

We next consider partitioning of energy between the CH_3 rotational energy and the spin−orbit energy of $O(^3P_j)$ (eq 3). As shown in column 3 of Table 1, the peak widths of each vibrational component increase monotonically in the 3_0^n progression for $n \geq 7$, denoting increasing rotational and/or spin−orbit product excitation. Although we present the rotational envelope widths for the two limiting cases in which no energy or a statistical distribution of energy is deposited in the oxygen atom, there is no reason to believe that either limit reflects reality, or that the spin−orbit state distribution is independent of photon energy, as our two limiting cases assume. Indeed, by analogy with the spin−orbit distributions measured in O_2 dissociation[65] it is likely that the j distributions of the oxygen atoms from CH_3O are not statistical but fluctuate in a seemingly random fashion depending the value of n. Subject to this assumption, we conclude that the increasing peak widths in Table 1 reflect an increase of rotational excitation as a function of photon energy.

However, the amount of the available energy deposited in product rotation is still relatively small. For example, in the 3_0^{10} $P(E_T)$ distribution (Figure 6), the energy difference between $CH_3(v = 0, J = 0, K = 0)$ and the peak of the $CH_3(v = 0)$ distribution is 50 meV (6% of the available energy). This energy corresponds to the rotational energy of a $CH_3(v = 0, J = 6, K = 0)$ fragment when the cofragment is $O(^3P_2)$; an excited O atom would require even smaller rotational quantum numbers for CH_3. Simply put, the fact that we resolve vibrational structure at all in the $P(E_T)$ distributions means that product rotational excitation is not extensive. We propose that the small amount of product rotation indicates a dissociation pathway which deviates little from C_{3v} symmetry for 3_0^n excitation.

In contrast to the $P(E_T)$ distributions just discussed, the distributions for 3_0^6 and $3_0^n 6_0^1$ lack the well-resolved vibrational features present in the other spectra in Figure 6. For 3_0^6, the much broader vibrational peak is likely due to an experimental effect rather than an increase in rotational excitation with respect to 3_0^7. The most recent literature value for the fluorescence lifetime of 3_0^6 is 0.37 μs,[44] a substantial fraction of the 9 μs flight time required for a CH_3O radical with 8 keV energy to travel from the dissociation laser to the TPS detector. Excited state lifetimes in this range degrade the $P(E_T)$ distributions to lower E_T because long-lived radicals remain intact for a portion of the flight time, resulting in a smaller recoil vector measured at the detector, which translates to an artificially small value of E_T for that event. Using the fluorescence lifetime given above, this effect causes a $1/e$ broadening of 51 meV.[66] When this width is deconvoluted from the 68 meV width given in Table 1, the remaining rotational envelope has a width of 45 meV, slightly narrower than the 47 meV width measured for 3_0^7. Therefore, rotational excitation of the $CH_3 + O$ products following 3_0^6 excitation follows the same trend as the other members in the 3_0^n progression despite the broad peak observed in Figure 6.

The $P(E_T)$ distributions following $3_0^6 6_0^1$ and $3_0^7 6_0^1$ excitation show broader peaks than their quasi-isoenergetic counterparts in the 3_0^n progression. Powers *et al.*[44] found that the fluorescence lifetime for $3_0^6 6_0^1$ lies between the limits 20 ns $\geq \tau_{FL} \geq$ 20 ps. As a result of this short lifetime, the broadening effect described above for 3_0^6 is negligible compared to the experimental resolution, and the increased width of the peaks is likely a result of greater product rotational excitation. The observation of rotational broadening is reasonable when one considers that the ν_6 methyl rocking motion would naturally develop into rotational excitation of the methyl radical about the b-axis, and supports the assignment that the combination band in Figure 4 is principally $3_0^n 6_0^1$ rather than $3_0^n 5_0^1$.

The product angular distributions for $3_0^6 6_0^1$ and $3_0^7 6_0^1$ excitation are described by anisotropy parameters of $\beta = 0.4$ and $\beta = 0.3$, respectively, while the angular distributions of the 3_0^n progression are isotropic ($\beta = 0$). However, the $\tilde{A}(^2A_1) \leftarrow \tilde{X}(^2E)$ transition has a perpendicular transition dipole moment, which should result in an anisotropy parameter $\beta \leq 0$. Although the vibronic symmetry of $3_0^n 6_0^1$ is parallel (e ← e), the electronic part of the transition dipole remains (a ← e) in the absence of perturbations by other electronic states,[30] and hence should still give $\beta \leq 0$. Therefore the positive values of β measured for $3_0^6 6_0^1$ and $3_0^7 6_0^1$ excitation implies that the $\tilde{A}$ state is perturbed by another electronic state of e symmetry (such as the nearby ^4E state shown in Figure 2), which mixes an electronic e ← e component into the transition dipole. These results are consistent with the observation of both parallel and perpendicular rotational structure resolved in CH_3O bands containing fundamentals of e vibrations.[30]

2. $CD_3 + O$ Products. The $P(E_T)$ distributions for the C−O bond fission channel in CD_3O show two main differences from the CH_3O distributions. First, the CD_3 vibrational distributions resulting from 3_0^n excitation are substantially more excited than at similar photon energies in CH_3O, as verified by comparison of the average product vibrational energies $\langle E_V \rangle$ in Tables 1 and 2. Second, the CD_3 vibrational distributions resulting from $3_0^n 2_0^1$ excitation are bimodal, as shown in Figure 7.

Increased vibrational excitation of the CD_3 umbrella motion resulting from 3_0^n excitation follows directly from the adiabatic dissociation mechanism proposed for channel I dynamics in CH_3O. When H atoms are replaced with D atoms in methoxy, the increased mass inhibits the ability of these atoms to track the motion of the C and O atoms during dissociation. As a result, the dissociation is less vibrationally adiabatic, resulting in more excitation of the ν_2 mode in CD_3.

A similar isotope effect is observed in CD_3I dissociation, and the complete description of these effects found in Ref. 64 is most likely applicable to CD_3O. However, for the present purposes, the simple explanation given above is sufficient.

By far the most surprising result from the CD_3O $P(E_T)$ distributions is the bimodal CD_3 product state distribution observed following excitation of the $3_0^n 2_0^1$ combination band (*cf.* Table 2). To the best of our knowledge, methoxy photodissociation represents the first observation of such an isotope effect on the *product* state distributions. A compelling hypothesis for the origin of this dynamical effect lies in the near equality between the umbrella mode frequency in the $\tilde{A}$ state of CD_3O (971 cm^{-1}) and the corresponding first overtone frequency of the umbrella mode in the CD_3 fragment $2\nu_2(CD_3) = 966\ cm^{-1}$.[61] Therefore, if the single quantum of $\nu_2(CD_3O)$ excited in the $3_0^n 2_0^1$ combination band does not couple well to the reaction coordinate, the 971 cm^{-1} of energy deposited into this motion will result in a propensity to populate the nearly degenerate first overtone of $\nu_2(CD_3)$, *i.e.*, the amount of energy in umbrella motion will be conserved throughout the dissociation. This hypothesis is also supported by the fact that $3_0^5 2_0^1$ does not dissociate (*cf.* Figure 5), even though this state has more energy than the 3_0^6 level, which does dissociate. This intriguing hypothesis calls for a comparison with reaction dynamics calculations based on the new potential energy surfaces which are now becoming available for methoxy.[39,40]

3. Curve-Crossing mechanism. Until now we have discussed the dissociation dynamics without consideration of the mechanism that couples the optically accessed $\tilde{A}(^2A_1)$ state with the $^4A_2$, ^4E, and $^2A_2$ repulsive states. The calculations of Jackels demonstrated that the ^4E state is reached *via* a one-electron transition from the Ã state, while the two A_2 configurations require the rearrangement of two electrons.[33] He argued that the $^2A_1 \Leftrightarrow {}^4E$ interaction should be the strongest, because these states have a first-order spin−orbit interaction, analogous to that of the $^2\Sigma \Leftrightarrow {}^4\Pi$ coupling in a diatomic radical. The $^2A_1 \Leftrightarrow {}^4A_2$ interaction can occur by a second-order spin−orbit interaction, while the $^2A_1 \Leftrightarrow {}^2A_2$ interaction is most likely dominated by off-diagonal elements in the nuclear kinetic energy operator.

Recent *ab initio* calculations by Pederson and Yarkony,[39] and by Cui and Morokuma[40] have defined the minimum seam of crossings between the Ã state and each repulsive curve. The new calculations place the crossing points at lower energy than those obtained by Jackels, in better agreement with our photodissociation threshold. The coupling constants between the states are also calculated, along with the dependence of the coupling at geometries away from C_{3v} symmetry.[39]

Until now, the experimental data has been discussed for simplicity under the tacit assumption that one repulsive curve accounts for the entire dynamics of channel I. Two features in Figure 6 may shed some light on whether coupling with multiple curves contributes to the final product state distributions. First, the $P(E_T)$ distribution following 3_0^7 excitation is much narrower than the 3_0^6 distribution, indicating a substantial increase in dissociation rate at the higher of these two photon energies (see section V.B.1.). One hypothesis for the increased dissociation rate is that the 3_0^6 distribution is mediated primarily by the $^4A_2$ surface, while the 3_0^7 distribution contains a new contribution from the ^4E surface. This picture agrees with Jackel's argument that coupling with the ^4E surface is stronger than coupling to the other two repulsive surfaces. However, it is also possible that dissociation following 3_0^6 excitation may require tunneling through a small barrier, while at 3_0^7 dissociation occurs without a barrier. A second noteworthy feature from Figure 6 is that the CH_3 vibrational excitation resulting from 3_0^{13} excitation is bimodal (*cf.* Table 1), which could plausibly result from the contribution of an additional repulsive curve at this high photon energy leading to vibrationally cold products. Detailed assessment of these issues should soon be possible in light of the new potential energy surfaces being developed.

C. Channel II−IV Dissociation Mechanisms. Our experimental information on the $CH_2 + OH$ product channel is limited. We find that this product channel is absent for transitions with $h\nu < 37\,500$ cm^{-1} and competes with the dominant $CH_3 + O$ channel at higher photon energies. As pointed out in section IV.B on energetic grounds it appears that channel III, producing electronically excited methylene fragments, dominates production of ground state methylene, channel II. Concerning the mechanism for this channel, the recent *ab initio* study of the methoxy system by Cui and Morokuma[40] explored the excited state isomerization of $CH_3O \rightarrow CH_2OH$, finding a transition state 1.00 eV above the Ã state minimum. They point out that the Ã state of CH_3O correlates through this transition state to channel III products, while the X̃ state correlates to channel II products. Our data are consistent with the excited state mechanism, and the observed production of some ground state methylene could easily be explained by a transition to a lower surface along the isomerization or dissociation coordinate. A similar mechanism is probably responsible for $CD_2 + OD$ dissociation in CD_3O.

Cui and Morokuma also found a substantial barrier to formation of $H + CH_2O$ on excited state surfaces, in contrast to the small barrier on the ground state for this channel. The fact that we observe very little $H + CH_2O$ is consistent with their result, indicating that all the dynamics in ultraviolet methoxy dissociation occur on excited state surfaces.

VI. Conclusions

The ultraviolet $\tilde{A}(^2A_1) \leftarrow \tilde{X}(^2E)$ transition in both CH_3O and CD_3O is observed to predissociate due to curve crossings with one or more of the excited $^4A_2$, ^4E, and $^2A_2$ repulsive states. Several interesting differences in the photodissociation dynamics have been observed between the two isotopes. The photofragment yield spectrum of CH_3O shows a main progression in the C−O stretch and a combination band with one quantum of the e symmetry ν_6 methyl rock. The 3_0^n progression also dominates in CD_3O, but the $3_0^n2_0^1$ is the most prominent combination band involving the a_1 symmetry ν_2 umbrella motion. The 3_0^6 transition is the lowest energy transition observed to dissociate in either isotope, placing the threshold for CH_3O dissociation 3775 cm^{-1} above the zero point level of the Ã state. In CH_3O the combination band $3_0^n6_0^1$ dissociates for $n = 5$, while in CD_3O combination band dissociation is not observed unless $n \geq 6$. This mode-specific effect demonstrates that the way in which energy is distributed in the Ã state effects the competition between dissociation and fluorescence.

The major product channel is C−O bond fission giving a methyl radical and an oxygen atom. The translational energy distributions for both isotopes show that the ν_2 umbrella mode of the $CH_3(CD_3)$ fragment is excited, although most of the available energy is channeled into product translation. The photofragment vibrational distributions lie much closer to the adiabatic limit than the sudden limit, indicating that the light H atoms can follow dissociation along the C−O bond distance; this picture is less accurate for CD_3O than CH_3O, as expected. Excitation of $3_0^n6_0^1$ in CH_3O results in more rotational excitation of the products, consistent with sampling of non-C_{3v} geometries in the Ã state. Excitation of $3_0^n2_0^1$ in CD_3O shows a surprising dynamical effect: the product state distribution of the CD_3 fragment is bimodal, with excitation of $v_2 = 0$ and $v_2 = 2$ always greater than that for $v_2 = 1$. This effect is clear evidence that the energy distribution among parent vibrational modes has a strong effect on the vibrational distribution in the products.

The results given in this article should enable a rigorous comparison between experiment and theory because the data comprise *both* translational and vibrational product state distributions, acquired at many different photon energies for two isotopes. New *ab initio* potential energy surfaces are now becoming available for methoxy, and it appears that the methoxy radical will continue its tradition as a benchmark molecule in the fields of spectroscopy and dynamics.

Acknowledgment. This research is supported by the Director, Office of Energy Research, Office of Basic Energy Science, Chemical Sciences Division of the US Department of Energy on Contract DE-AC03-76SF00098.

References and Notes

(1) Style, D. W. G.; Ward, J. C. *Trans. Faraday Soc.* **1953**, *49*, 999.

(2) Leighton, P. H. *Photochemistry of Air Pollution*; Academic Press: New York, 1961. Finlayson-Pitts, B. J.; Pitts, J. N., Jr. *Atmospheric Chemistry*; Wiley: New York, 1986. Pate, C. T.; Finlayson, B. J.; Pitts, J. N., Jr. *J. Am. Chem. Soc.* **1974**, *96*, 6554. Levy, H. II *Planet. Space Sci.* **1973**, *21*, 575. Baldwin, A. C.; Barker, J. R.; Golden, D. M.; Hendry, D. G. *J. Phys. Chem.* **1977**, *81*, 2483.

(3) Westbrook, C. K.; Dryer, F. L. *Prog. Energy Combust. Sci.* **1984**, *10*, 1. Tsang, W.; Hampson, R. F. *J. Phys. Chem. Ref. Data* **1986**, *15*, 1087. Williams, B. A.; Fleming, J. W. *Chem. Phys. Lett.* **1994**, *221*, 27. Zabarnick, S. *Combust. Flame* **1991**, *85*, 27. Olsen, D. B.; Gardiner, W. C., Jr. *J. Phys. Chem.* **1977**, *81*, 2514.

(4) Warnatz, J. *Combustion Chemistry*; Gardiner, W. C., Ed.; Springer: Berlin, 1984; p 258.

(5) Thaddeus, P. Private communication.

(6) Geers, A.; Kappert, J.; Temps, F.; Wiebrecht, J. W. *J. Chem. Phys.* **1993**, *99*, 2271. *Ibid*. **1994**, *101*, 3618. *Ibid*. **1994**, *101*, 3634.

(7) Osborn, D. L.; Leahy, D. J.; Ross, E. R.; Neumark, D. M. *Chem. Phys. Lett.* **1995**, *235*, 484.

(8) Ohbayashi, K.; Akimoto, H.; Tanaka, I. *J. Phys. Chem.* **1977**, *81*, 798.

(9) Engelking, P. C.; Ellison, G. B.; Lineberger, W. C. *J. Chem. Phys.* **1978**, *69*, 1826.

(10) Wendt, H. R.; Hunziker, H. E. *J. Chem. Phys*. **1979**, *71*, 5202.

(11) Russell, D. K.; Radford, H. E. *J. Chem. Phys*. **1980**, *72*, 2750.

(12) Inoue, G.; Akimoto, H.; Okuda, M. *J. Chem. Phys*. **1980**, *72*, 1769.

(13) Powers, D. E.; Hopkins, J. B.; Smalley, R. E. *J. Phys. Chem*. **1981**, *85*, 2711.

(14) Endo, Y.; Saito, S.; Hirota, E. *J. Chem. Phys*. **1984**, *81*, 122.

(15) Carrick, P. G.; Brossard, S. D.; Engelking, P. C. *J. Chem. Phys*. **1985**, *83*, 1995.

(16) Fuke, K.; Ozawa, K.; Kaya, K. *Chem. Phys. Lett*. **1986**, *126*, 119.

(17) Ebata, T.; Yanagishita, H.; Obi, K.; Tanaka, I. *Chem. Phys*. **1982**, *69*, 27.

(18) Agrawalla, B. S; Setser, D. W. *J. Phys. Chem*. **1986**, *90*, 2450.

(19) McCaulley, J. A.; Anderson, S. M.; Jeffries, J. B.; Kaufman, F. *Chem. Phys. Lett*. **1985**, *115*, 180.

(20) Brossard, S. D.; Carrick, P. G.; Chappell, E. L.; Hulegaard, S. C.; Engelking, P. C. *J. Chem. Phys*. **1986**, *84*, 2459.

(21) Garland, N. L; Crosley, D. R. *J. Phys. Chem*. **1988**, *92*, 5322.

(22) Lin, S. R.; Lee, Y. P.; Nee, J. B. *J. Chem. Phys*. **1988**, *88*, 171.

(23) Foster, S. C.; Misra, P.; Lin, T. Y. D.; Damo, C. P.; Carter, C. C.; Miller, T. A. *J. Phys. Chem*. **1988**, *92*, 5914.

(24) Chiang, S. Y.; Hsu, Y. C.; Lee, Y. P. *J. Chem. Phys*. **1989**, *90*, 81.

(25) Liu, X.; Damo, C. P.; Lin, T. Y. D.; Foster, S. C.; Misra, P.; Yu, L.; Miller, T. A. *J. Phys. Chem*. **1989**, *93*, 2266.

(26) Liu, X.; Foster, S. C.; Williamson, J. M.; Yu, L.; Miller, T. A. *Mol. Phys*. **1990**, *69*, 357.

(27) Misra, P.; Zhu, X.; Hsueh, C.; Halpern, J. B. *Chem. Phys*. **1993**, *178*, 377.

(28) Lee, Y. Y.; Wann, G. H.; Lee, Y. P. *J. Chem. Phys*. **1993**, *99*, 9465.

(29) Williams, B. A.; Fleming, J. W. *Chem. Phys. Lett*. **1994**, *221*, 27.

(30) Powers, D. E.; Pushkarsky, M.; Miller, T. A. *J. Chem. Phys.* **1997**, *106*, 6863.

(31) Temps, F. Unpublished.

(32) Yarkony, D. R.; Schaefer, H. F.; Rothenberg, S. *J. Am. Chem. Soc*. **1974**, *96*, 656.

(33) Jackels, C. F. *J. Chem. Phys*. **1982**, *76*, 505. *Ibid*. **1985**, *82*, 311.

(34) Bent, G. D.; Adams, G. F.; Bartram, R. H.; Purvis, G. D.; Bartlett, R. J. *J. Chem. Phys*. **1982**, *76*, 4144.

(35) Carter, J. T; Cook, D. B. *J. Mol. Struct.* (*THEOCHEM*) **1991**, *251*, 111.

(36) Curtiss, L. A.; Kock, L. D.; Pople, J. A. *J. Chem. Phys*. **1991**, *95*, 4040.

(37) Walch, S. P. *J. Chem. Phys*. **1993**, *98*, 3076.

(38) Bent, G. D. *J. Chem. Phys*. **1994**, *100*, 8219.

(39) Pederson, L.; Yarkony, D. Private communication.

(40) Cui, Q; Morokuma, K. *Chem. Phys. Lett.* **1996**, *263*, 54.

(41) Englman, R. *The Jahn-Teller Effect in Molecules and Crystals*; Wiley: New York, 1972.

(42) Geers, A.; Kappert, J.; Temps, F. *J. Chem. Phys*. **1993**, *98*, 4297.

(43) Hougen, J. T. *J. Mol. Spectrosc*. **1980**, *81*, 73. Watson, T. K.; *J. Mol. Spectrosc*. **1984**, *103*, 125. Brown, J. M. *Mol. Phys*. **1971**, *20*, 817. Ham, F. S. *Phys. Rev*. **1968**, *166*, 307.

(44) Powers, D. E.; Pushkarsky, M.; Miller, T. A. *J. Chem. Phys.* **1997**, *106*, 6878.

(45) Chase, M. W., Jr.; Davies, C. A.; Downey, J. R., Jr.; Frurip, D. J.; McDonald, R. A.; Syverud, A. N. JANAF Thermochemical Tables, 3rd ed.; *J. Chem. Phys. Ref. Data* **1985**, *14*, (Suppl. 1).

(46) Osborn, D. L.; Choi, H.; Mordaunt, D. H.; Bise, R. T.; Neumark, D. M.; Rohlfing, C. M. *J. Chem. Phys.* **1996**, *106*.

(47) Continetti, R. E.; Cyr, D. R.; Osborn, D. L.; Leahy, D. J.; Neumark, D. M. *J. Chem. Phys*. **1993**, *99*, 2616.

(48) Continetti, R. E.; Cyr, D. R.; Metz, R. B.; Neumark, D. M. *Chem. Phys. Lett*. **1991**, *182*, 406.

(49) Osborn, D. L.; Leahy, D. J.; Cyr, D. R.; Neumark, D. M. *J. Chem. Phys*. **1996**, *104*, 5026.

(50) Bakker, J. M. B. *J. Phys. E* **1973**, *6*, 785; *ibid*. **1974**, *7*, 364.

(51) Gerstenkorn, S.; Luc, P. *Atlas du Spectre d'Absorption de la Molecule d'Iode*; Centre National de la Recherche Scientifique: Paris, 1978.

(52) Leahy, D. J.; Osborn, D. L.; Cyr, D. R.; Neumark, D. M.; *J. Chem. Phys*. **1995**, *103*, 2495.

(53) de Bruijn, D. P; Los, J. *Rev. Sci. Instrum*. **1982**, *53*, 1020.

(54) Zare, R. N. *Mol. Photochem*. **1972**, *4*, 1.

(55) Osborn, D. L.; Choi, H.; Mordaunt, D. H.; Bise, R. T.; Neumark, D. M.; Rohlfing, C. M. *J. Chem. Phys.* **1997**, *106*, 10087.

(56) Osborn, D. L.; Leahy, D. J.; Kim, E. H.; deBeer, E.; Neumark, D. M. In preparation.

(57) Yamada, C.; Hirota, E.; Kawaguchi, K. *J. Chem. Phys*. **1981**, *75*, 5256. Yamada, C.; Hirota, E. *Ibid*. **1983**, *78*, 669. Herman, H. W; Leone, S. R. *J. Chem. Phys*. **1982**, *76*, 4759.

(58) The function $f_n(E_T)$ is a convolution of a Gaussian with a Boltzmann distribution. The FWHM of $f_n(E_T)$ is nearly identical to its Gaussian component. The use of a Boltzmann component does not imply rotational equilibrium but is simply a convienent mathematical form to provide a low-energy tail to $f_n(E_T)$.

(59) It should be noted that the value for the parameter Δ scales roughly with the value of Γ; together they control the amount of rotational and spin−orbit energy in the model.

(60) Moore, C. E. *Atomic Energy Levels*; NSRDS-NBS Circular No. 467; U.S. GPO: Washington, DC, 1949; Vol. 1 p 15.

(61) Sears, T. J.; Frye, J. M; Spirko, V.; Kraemer, W. P. *J. Chem. Phys*. **1989**, *90*, 2125.

(62) $\Delta H^\circ_{f,0}(CD_3)$ is derived as $\Delta H^\circ_{f,0}(CD_3) = \Delta H^\circ_{f,0}(CD_3) - [ZPE(CH3) - ZPE(CD3)] + 3/2[ZPE(H2) - ZPE(D2)]$, where the zero-point energies for the methyl radicals are taken from ref 61.

(63) Schinke, R. *Photodissociation Dynamics*; Cambridge University Press: Cambridge, 1993.

(64) Amatatsu, Y.; Morokuma, K.; Yabushita, S. *J. Chem. Phys*. **1991**, *94*, 4858. *Ibid*. **1996**, *104*, 9783.

(65) Leahy, D. J.; Osborn, D. L.; Cyr, D. R.; Neumark, D. M. *J. Chem. Phys*. **1995**, *103*, 2495.

(66) For comparison, a 10 ns fluorescence lifetime gives a 1/*e* broadening of 1 meV, a negligible value compared to the instrumental resolution.